Accelerated thermal history analysis of light-burnt magnesium oxide by surface properties

Results in Materials 17 (2023) 100368

Contents lists available at ScienceDirect

Results in Materials

journal homepage: www.sciencedirect.com/journal/results-in-materials

Accelerated thermal history analysis of light-burnt magnesium oxide by surface properties

H. Karimi *, H.J.H. Brouwers

Department of the Built Environment, Eindhoven University of Technology, P.O. Box 513, 5600 MB Eindhoven, the Netherlands

ARTICLE INFO

Keywords:
Light-burnt magnesia
Homogeneity
Thermal history
Adsorption mechanism
Pore size distribution
Deconvolution

ABSTRACT

Homogeneity is of utmost importance in some applications of light-burnt magnesia (LBM), such as shrinkage compensation of cement composites, because if it is not detected reliably before application, it causes unpredicted expansion and cracking. This paper presents an accelerated method for homogeneity and thermal history detection in LBM. The proposed method provides an equation for computing the weighted mesopore probability distribution of light-burnt magnesia (LBM). Then, it deconvolutes the distribution's peaks by Lorentz peak functions to analyze homogeneity. The method's performance is evaluated by examining LBM samples produced by calcining magnesite at four temperatures and walking through several scenarios, including the mixtures of these samples. The results confirmed that the method accurately detects inhomogeneity and gives calcination temperatures and percentages of fractions of magnesia mixtures. These findings make it possible to prevent unpredicted expansion in cement composites incorporating expansive magnesia and can be employed to detect inhomogeneities in other porous materials applications.

1. Introduction

Magnesia (MgO) is relatively rare in nature and is usually produced by the thermal decomposition of magnesium compounds such as magnesite ($MgCO_3$) [1]. The magnesia production industry is projected to grow at a rate of 5% from 2021 to 2031 [2], and global magnesite mine production was about 28 million metric tons (Mt) in 2020 [3]. Magnesia has a wide variety of applications ranging from manufacturing refractories [4–7], catalysts [8,9], rubber [10], and plastic to wastewater treatment [11] and air pollution control [12]. Existing research has shown the influence of manufacturing source [13–15], manufacturing method [16–18], manufacturing atmosphere [19], calcination process and sintering [20–25], calcination kinetics [26], and crystal orientation [27–29] on the properties of magnesia.

Light-burnt magnesia (LBM) is usually produced by calcining magnesite at temperatures lower than 1000 °C. It accounts for one-third of magnesia applications and has high chemical activity. LBM has two significant applications in construction industry: Firstly, it is used as an expansive agent to compensate shrinkage of concrete. Carefully calcined LBM acts as an expansive agent and produces expansion at a rate closely matching the long-term shrinkage of concrete to prevent concrete cracking [30]. Secondly, LBM is used as a primary ingredient to produce Sorel cements. More information on the application of LBM in concrete is provided in the recent reviews by Walling and Provis [31], Mo et al. [32] and Du [33]. It is now well established that variation in the thermal history of LBM, significantly affects the properties of the final application products [34]. Cao et al. specified the importance of information on the thermal history of LBM and introduced an LBM reactivity assessment technique based on reaction with an ethylic buffer solution [35]. They studied the hydration characteristics and expansive mechanism of LBM [36] and evaluated the hydration procedure of LBM on the expansive behavior of shrinkage-compensating mortar [37].

Much of the current literature on LBM pays particular attention to the assessment of the average reactivity of LBM. Mo et al. [38] studied calcination of magnesium oxides and reported the change in porosity and crystal structure of magnesia due to calcination temperature. Harper used iodine number to index reactivity as used by American magnesia industry [23]. Alegret et al. [39] proposed potentiometry to study reactivity of magnesia. Hirota et al. [40] characterized sintering of magnesia by crystallite size, particle size, and morphology. Kim et al. [41] studied the transformation of the crystal structure of $MgCO_3$ and $Mg(OH)_2$ to MgO during calcination. Zhu et al. [42] proposed a corrected MgO hydration convention method for reactivity assessment. Chau et al. [43] introduced an accelerated reactivity assessment method based on the time required for acid neutralization of magnesia.

* Corresponding author.
E-mail address: h.karimi@tue.nl (H. Karimi).

https://doi.org/10.1016/j.rinma.2023.100368
Received 3 November 2022; Received in revised form 23 December 2022; Accepted 9 January 2023
Available online 11 January 2023

Nomenclature

A	area of the Lorentz peak function
$A_{fraction\ i}^{cumulative}$	area of the ith Lorentz fit in the cumulative fit
$A_{fraction\ i}^{unmixed}$	area of the ith Lorentz fit in its unmixed form
a_{BET}	BET surface area
$a_{\alpha s}$	calculated surface area of the test material from the α_s curve
a_{BET}^{ref}	BET surface area of the standard data
C	BET constant
$C(w_i)$	cumulative mesopore size distribution
$I_{(w)}$	the incremental mesopore size distribution
L	Avogadro constant
$L(w_i)$	weighted mesopore probability distribution
m^s	mass of adsorbing solid sample (g)
$N_{exp}\left(p/p^0\right)$	measured number of adsorbed molecules
N_{theo}	kernel of theoretical isotherms in model pores
p	actual adsorbing gas pressure (mmHg)
p^0	saturation pressure of the adsorbing gas (mmHg)
$P(w_i)$	mesopore probability distribution (probability density function)
s_{ref}	slope of the α_s plot of the standard data
s_{test}	slope of the α_s plot of the test material
T	thermodynamic temperature
V^a	amount of adsorbate (cm^3/g STP)
V_{ref}^a	amount of adsorbate in the standard data
$V_{ref}^{0.4}$	amount of adsorbate at the pre-selected relative pressure of 0.4 in the standard data
V_m	monolayer capacity (cm^3/g STP)
V_0	gas molar volume (22,414 cm^3)
$V_{tot,m}$	total mesopore volume
W	full width at half maximum (FWHM)
w	pore width (nm)
w_i	the ith mesopore width
y_0	offset from the y-axis in Lorentz peak function
δV_i	the ith mesopore volume increment
δw_i	the ith mesopore width increment
σ	mean molecular cross-sectional area

Abbreviations

BET	Brunauer–Emmett–Teller
FWHM	Full width at half maximum
IUPAC	International Union of Pure and Applied Chemistry
NLDFT	Nonlocal density functional theory
LBM	Light-burnt magnesia
PDF	Probability density function
XRD	X-ray Diffraction

Surprisingly, none of the current LBM reactivity analysis methods provides information on thermal history.

The current study aims at filling this research gap by studying surface properties and analyzing the highly porous structure of LBM formed during calcination. This highly porous structure is thanks to the pseudomorphous calcination of magnesite and is identifiable by gas physisorption techniques [44–47]. Here, the nonlocal density functional theory (NLDFT) is used to compute the mesopore size distribution of LBM. NLDFT allows a better explanation of the adsorption and phase transitions in small mesopores, compared to classical Kelvin equation-based methods [48,49]. The proposed method provides an equation that weights this NLDFT data to compute the weighted mesopore probability distribution and deconvolutes the peaks of the distribution by Lorentz peak functions.

Four LBM samples are produced by the calcination of magnesite at 600 °C, 700 °C, 800 °C, and 900 °C. First, their adsorption mechanisms are studied by analyzing physisorption isotherm, BET surface area, C parameter, and alpha-s method. The samples' pore size distributions are computed by using nonlocal density functional theory (NLDFT). Next, their weighted mesopore probability distributions are computed and curve-fitted by Lorentz peak functions. Then, the weighted mesopore probability distributions of several scenarios, including the mixtures of these LBM samples, are analyzed. Finally, the distributions are deconvoluted by Lorentz peak functions, and a set of criteria for assessing homogeneity and thermal history of light-burnt magnesia is presented. This study shows how to use surface properties to characterize the thermal history of light-burnt magnesia, which is suitable for application in the construction field to produce Sorel cements and expansive magnesia.

2. Materials and methods

2.1. Materials

The current investigation involved producing light-burnt magnesia by thermal decomposition of magnesite at 600 °C, 700 °C, 800 °C, and 900 °C. The magnesite was obtained from the company Magnesia (Germany). The calcination was effected in a muffle furnace and the residence time was 24 h to ensure that the influence of residence time on the samples is negligible, and only calcination temperature controls the properties of samples. The calcination temperatures have been indicated in sample designations throughout this paper. For example, M600 refers to the sample calcined at 600 °C. Fig. 1 demonstrates the mineral crystalline phases of the samples, measured by X-ray Diffraction (XRD). The diffraction patterns were obtained using a Bruker ENDEAVOR diffractometer, equipped with a Co-radiation source, divergence slit (0.5°), soller slit (0.04 rad), and Lynxeye detector. The main crystalline phase of the samples is periclase. The main peak of periclase was utilized to compare the crystal grain sizes of the samples, using the Scherrer equation [50]. The average periclase crystallite size of M600 was 7.0 nm. The average periclase crystallite size of M700, M800, and M900 were 1.28 (9.0 nm), 1.68 (11.8 nm), and 1.93 (13.5 nm) times as big as those in M600, respectively. Fig. 2 exhibits the morphology of the

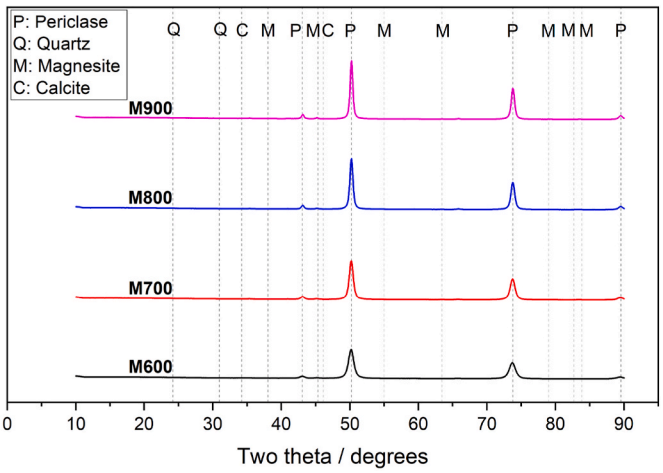

Fig. 1. The mineral crystalline phases of the samples measured by XRD (P: periclase, Q: quartz, M: magnesite, C: calcite).

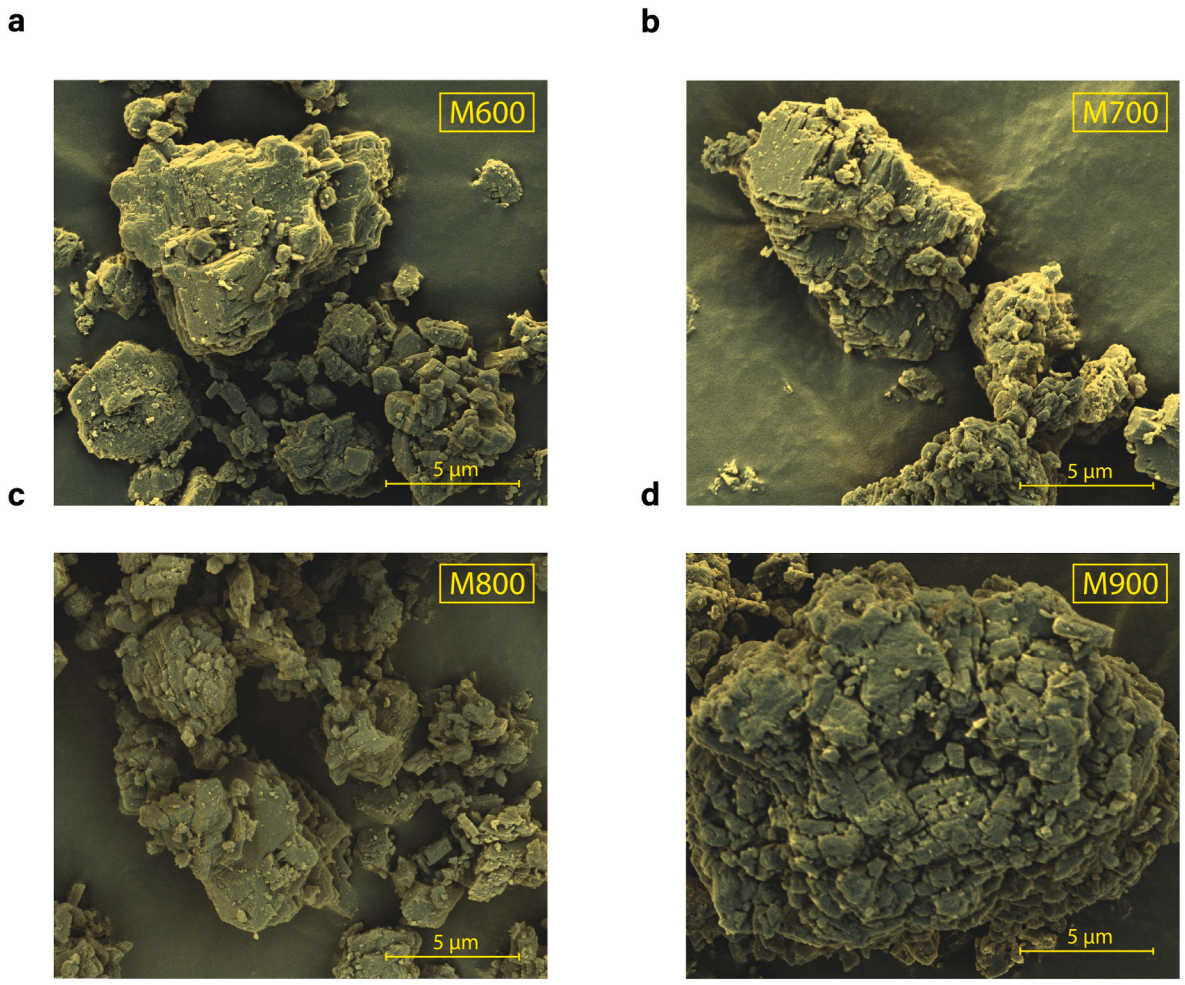

Fig. 2. Morphology and texture of the particles in LBM samples, obtained by ESEM: (a) M600; (b) M700; (c) M800, and (d) M900.

samples, taken by an environmental scanning electron microscope (ESEM). Micrographs were recorded by both secondary and backscattering electron detectors (MIX mode) at 5 kV with a spot of 3.0. In addition, four mixtures of LBM were prepared to investigate the applicability of the studied methods in characterizing homogeneity. Table 1 shows the composition of these mixtures.

2.2. Methodology

2.2.1. Adsorption mechanism

Before measuring physisorption isotherms, possible contaminants on the surface of the samples were removed by a combination of heat (120 °C) and flowing nitrogen gas for 4 h. When weighing the samples, a sample quantity that yields at least 10 m^2 was prepared for good precision. This amount ensured reasonable pressure difference thanks to sufficient gas adsorption by the adsorbent at each step [51].

After sample preparation, adsorption and desorption isotherms were measured at 77 K using a Micromeritics TriStar II analyzer. The adsorption isotherms were plotted using [48]

Table 1
The composition of LBM mixtures (in weight percent).

Item	M600	M800	M900
M600 (50%)+M800 (50%)	50%	50%	0
M600 (80%)+M800 (20%)	80%	20%	0
M600 (50%)+M900 (50%)	50%	0	50%
M600 (80%)+M900 (20%)	80%	0	20%

$$\frac{V^a}{m^s} = \mathrm{f}\left(\frac{p}{p^0}\right) T \tag{1}$$

with V^a the amount of adsorbate, m^s the mass of solid, p the actual adsorbing gas pressure, p^0 the saturation pressure of the adsorbing gas at T, and T the thermodynamic temperature [48]. Point B was shown on the measured physisorption isotherms as the point where the adsorption isotherms become linear [52].

In order to obtain the BET surface area, the linear transformed BET equation was used by the formula [48]

$$\frac{p}{V^a(p^0 - p)} = \frac{1}{V_m C} + \frac{C-1}{V_m C}\frac{p}{p^0} \tag{2}$$

with V^a the amount of adsorbed gas at the equilibrium pressure p, V_m the monolayer capacity, C a constant, and p and p^0 as used previously [48]. From Eq. (2), a plot of $\frac{p}{V^a(p^0-p)}$ versus $\frac{p}{p^0}$ was made to obtain a straight line with intercept $\frac{1}{V_m C}$ and slope $\frac{C-1}{V_m C}$ to calculate the values of V_m and C. The BET specific surface area then was calculated by [48]

$$a_{BET} = \frac{V_m \sigma L}{m^s V_0} \tag{3}$$

with σ the mean molecular cross-sectional area (0.163 nm^2 for nitrogen molecule), L the Avogadro constant (6.02214 × 10^{23} mol^{-1}), m^s the mass of adsorbing sample, V_0 the gas molar volume (22,414 cm^3), and V_m as used previously.

To obtain the surface area by α_s curve, the standard data of a

nonporous specimen were obtained from Bhambhani et al. [53]. Next, the α_s of the reference data was obtained from [52]

$$\alpha_s = \frac{V^a_{ref}}{V^{0.4}_{ref}} \tag{4}$$

with V^a_{ref} the amount of adsorbate in the standard data, and $V^{0.4}_{ref}$ the amount of adsorbate at the pre-selected relative pressure of 0.4 in the standard data.

Then, the α_s curve of the sample was constructed by specifying at similar relative pressures the value of α_s of the standard data and the value of V^a of the sample. Finally, a plot of V^a versus α_s was made to yield the α_s curve.

The surface area of samples was calculated from the α_s curve by [52]

$$a_{\alpha s} = \frac{s_{test}}{s_{ref}} \bullet a^{ref}_{BET} \tag{5}$$

with $a_{\alpha s}$ the calculated surface area of samples from the α_s curve, a^{ref}_{BET} the BET surface area of standard data, s_{test} the slope of the α_s plot of the test material, and s_{ref} the slope of the α_s plot of the standard data.

2.2.2. Pore structure

A complete mesopore size distribution was computed by the nonlocal density functional theory (NLDFT) method. In the NLDFT method, the pore size distribution was obtained by [48]

$$N_{exp}\left(\frac{p}{p^0}\right) = \int_{w_{min}}^{w_{max}} N_{theo}\left(\frac{p}{p^0}, w\right) \mathrm{f}(w)\mathrm{d}w \tag{6}$$

with $N_{exp}\left(\frac{p}{p^0}\right)$ the measured number of adsorbed molecules and N_{theo} the kernel of theoretical isotherms in model pores [48]. The computation procedure for pore size distribution by the NLDFT method can be found in Rouquerol et al. [48]. The NLDFT computations were done with a kernel, based on nitrogen adsorption at 77 K on graphitic carbon having slit-shaped pores, using the Tristar 3020 analysis program.

3. Results and discussion

3.1. Adsorption mechanism

The physisorption isotherms of the samples are displayed in Fig. 3. Each graph consists of adsorption and desorption isotherms. All the adsorption isotherms are initially concave, then become linear, and finally convex to the $\frac{p}{p^0}$ axis. All the desorption isotherms do not retrace the adsorption isotherms and create hysteresis loops. The hysteresis loops occur thanks to the intrinsic difference between the curvature of the liquid surface of condensate, from which the desorption occurs, and nucleation on the solid pore walls, from which multilayer adsorption and condensation starts [51]. This curvature hampers evaporation from the liquid surface, and therefore, the desorption isotherm falls behind the adsorption isotherm and leads to a hysteresis loop [51].

According to IUPAC recommendations, the general form of physisorption isotherms classifies adsorbents into six types [54]. Based on the measured physisorption data, all the four magnesia preparations belong to a Type IV-a class. Type IV isotherms initiate similar to Type II isotherms but have a characteristic plateau at higher relative pressures. They are a characteristic of mesoporous materials [48].

Fig. 4 illustrates the constitutive parts of Eq. (2) for calculating the

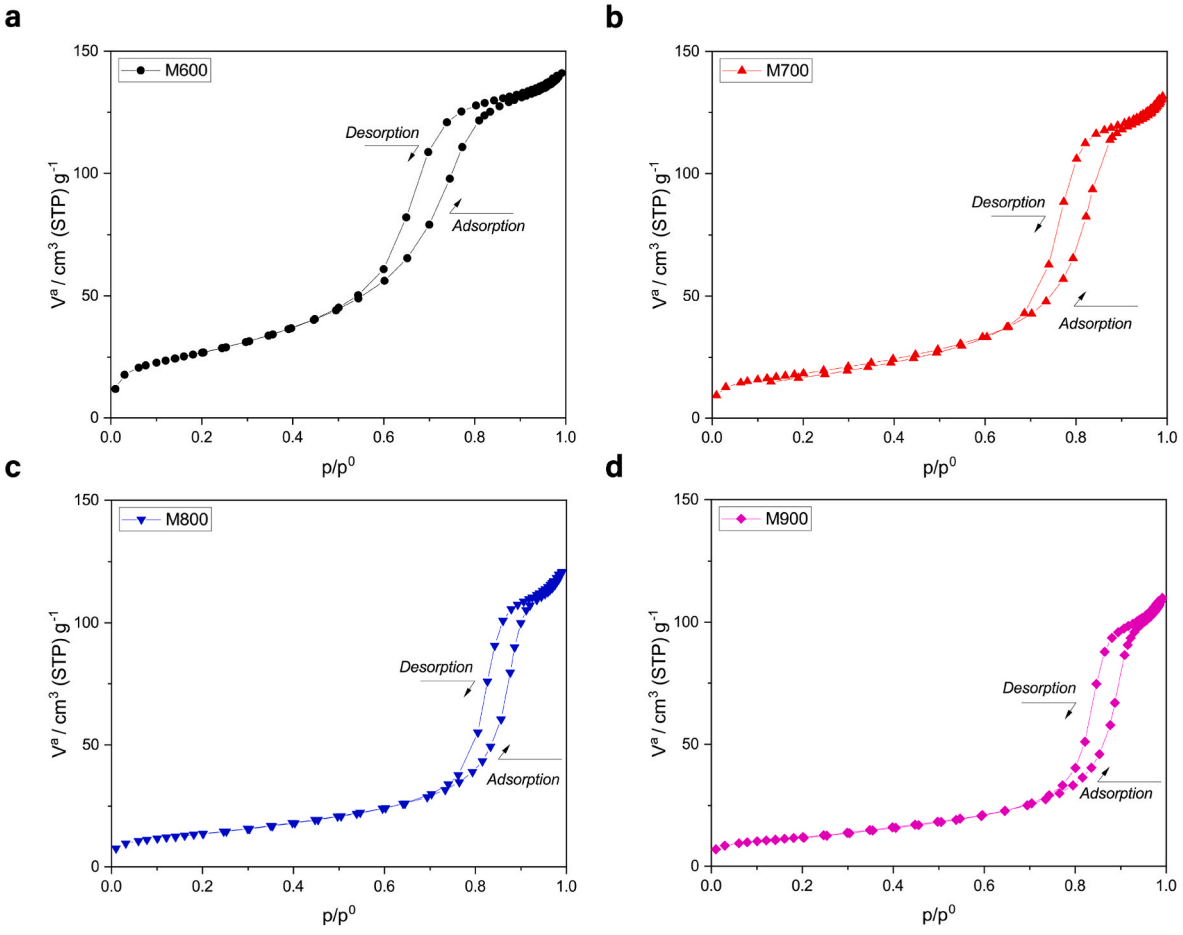

Fig. 3. Experimental adsorption and desorption isotherms of N_2 (at 77 K) on the LBM samples: (a) M600; (b) M700; (c) M800, and (d) M900.

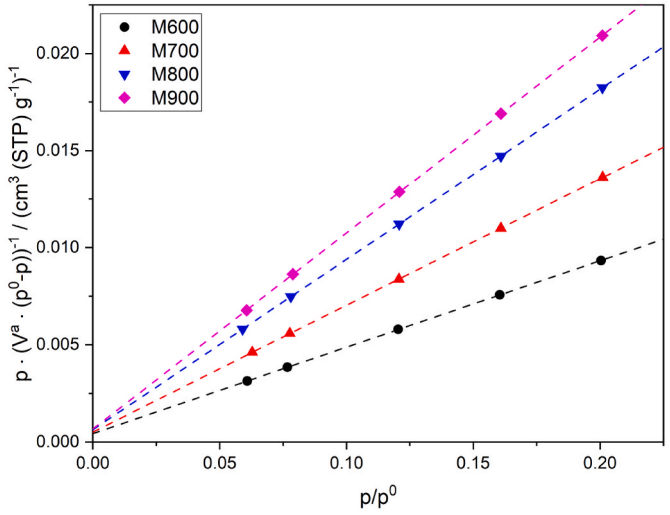

Fig. 4. BET plots of the LBM samples. The dashed lines represent the linear regression of the data.

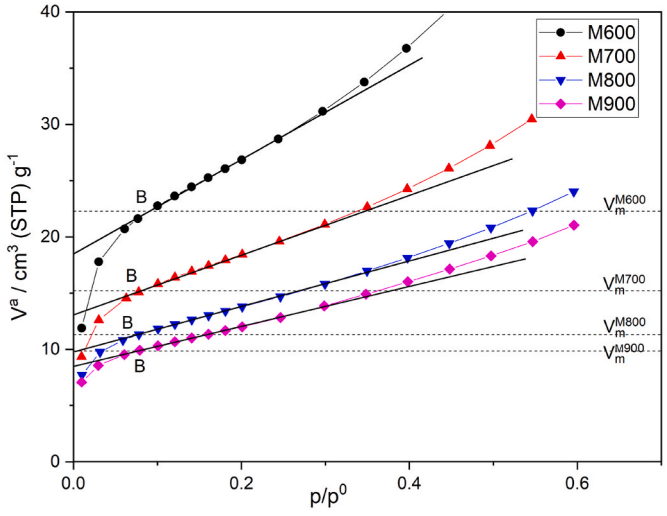

Fig. 5. Monolayer capacity (represented by dashed lines) and the Point B (represented by a point at the start of the linear section of adsorption isotherms) of the LBM samples.

BET surface area. The selected range of linearity of the BET plot was within the relative pressures of 0.05–0.2, according to Gregg and Sing [52]. All the preparations were well captured by the linear transformed BET model ($R^2 > 0.99$). As mentioned earlier, the y-intercept and the slope of the lines in Fig. 4 were used to calculate the monolayer capacity and C parameter from Eq. (2) and Eq. (3).

Table 2 compares and contrasts the BET surface area (a_{BET}) and C parameter of the samples. The BET surface area decreases with increasing calcination temperature. The parameter C provides useful information about the shape of the isotherm in the BET range. If the parameter C is less than 2, the competition between the gas-solid affinity and gas-gas affinity makes the BET method inapplicable [54]. On the other hand, a parameter C higher than 150 indicates high energy sites on the surface of micropores [54]. The beginning of the linear section of the adsorption isotherm indicates the monolayer completion and is usually referred to as Point B [54]. A parameter C of at least 80 indicates a rather explicit Point B [48,54]. The C parameter of M900 is just over 150, but as shown in Fig. 5, the monolayer capacity and Point B were in substantial agreement. The parameter C of the samples remains in the range of 80–150, Point B is demonstrable as a single point, and the value of monolayer capacity (V_m) is validated.

The first half of the adsorption isotherms of Fig. 3 are illustrated in Fig. 5. High energy sites on the surface of the samples cause the initial steep rise in the isotherms. This steep rise diminishes as the high-energy sites are covered. As predicted from the value of parameter C, the monolayer capacities of the samples (V_m), represented by horizontal dashed lines, are in substantial agreement with point B of the samples.

Fig. 6 shows the α_s plots of the samples. Inspection of these plots is instructive as there is a linear section in all the curves. Back-extrapolation of the linear sections gives near-zero intercept ($R^2 >$ 0.99 for the first eight points of each preparation). Zero intercept in α_s curves is an indication of a non-microporous sample. The upward deviation from the linear section in the curves is due to capillary condensation [48]. The calculated surface area of the samples (a_{as}) was determined by incorporating the slopes of these linear sections into Eq. (5). The results of this calculation are listed in Table 3.

Table 2
BET surface area and C parameter of LBM samples.

Item	M600	M700	M800	M900
BET surface area (a_{BET}) [m^2g^{-1}]	97.0	66.2	49.3	42.9
C parameter	103.9	130	140	152

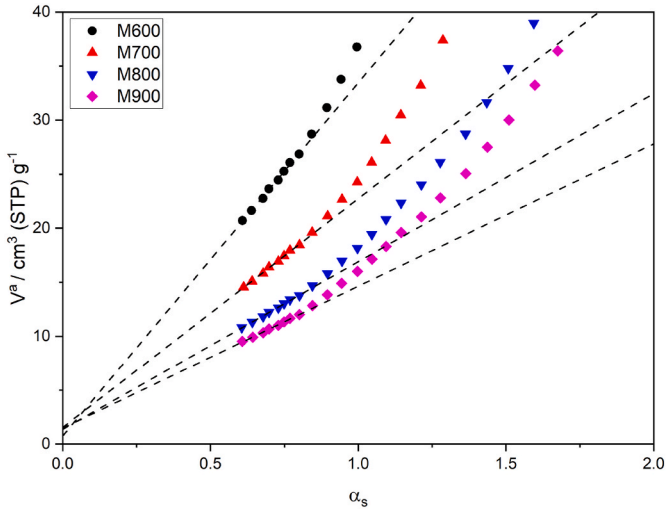

Fig. 6. α_s plots of the LBM samples. The dashed lines represent the back-extrapolation of the linear sections.

Table 3
Comparison of the calculated surface area from α_s plots with the BET surface area.

Item	M600	M700	M800	M900
Surface area from α_s plots (a_{as}) [m^2g^{-1}]	94.2	61.1	44.8	37.9
BET surface area (a_{BET}) [m^2g^{-1}]	97.0	66.2	49.3	42.9

The α_s curves give an independent evaluation of the total available surface area in a mesoporous material or the external area in a microporous material [48]. Table 3 compares the surface area (a_{as}), calculated from the physisorption isotherms and α_s plots, to the BET surface area. The small difference between the values of a_{as} and a_{BET} in the samples suggests that almost all the surface area in the samples is external and that the adsorption mechanism is mainly governed by mesopores.

3.2. Pore structure

As outlined earlier in the Introduction, the nonlocal density func-

tional theory (NLDFT) is implemented to compute the mesopore size distribution of LBM samples. The mesopore size distribution is [55]

$$I\,(w_i) = \delta V_{\mathrm{i}} \tag{7}$$

with δV_{i} the i-th mesopore volume increment, and $I\,(w_i)$ the mesopore size distribution. As can be seen in Fig. 7, on the whole, all the samples are highly mesoporous. This is explained by the pseudomorphous calcination of magnesite, in which magnesia retains the external shape and volume of magnesite [56,57] and is consistent with the studied adsorption mechanisms in the previous section. It is also apparent that the distributions shift to the right at higher calcination temperatures, and their peaks become smaller. The change in the pore structure of the samples at higher calcination temperatures is due to shrinkage and sintering [56,57] and is in line with the previously discussed change in the physisorption isotherms and surface area.

The cumulative mesopore size distribution of the samples is expressed by the sum of the mesopore volume increments in the form [55]

$$C(w_i) = \sum \delta V_{\mathrm{i}} \tag{8}$$

with $C(w_i)$ the cumulative mesopore size distribution and δV_{i} as used previously. As illustrated by Fig. 8, the pore structure alteration caused by shrinkage and sintering causes the total mesopore volume to decrease at higher calcination temperatures. It is also evident that the median mesopore width of the distribution shifts to the right at higher calcination temperatures.

In order to use the shift of the distributions in Figs. 7 and 8 to characterize the homogeneity of the samples, inspecting the probability

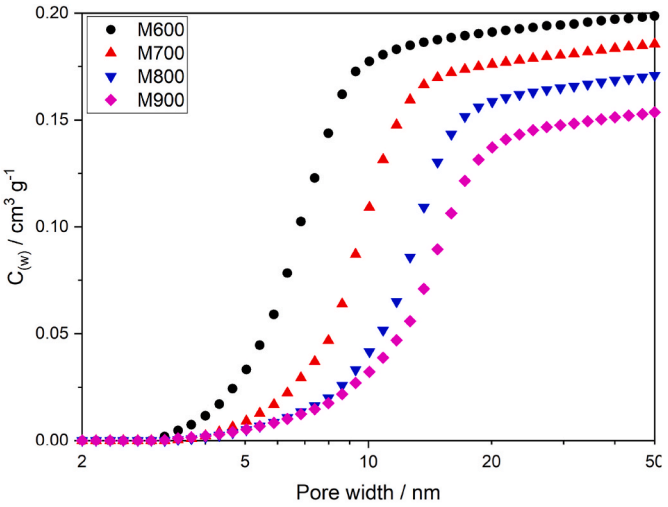

Fig. 8. Cumulative mesopore size distributions of the LBM samples, computed by Eq. (8).

density functions (PDFs) is constructive. The mesopore probability distribution of the samples is [55]

$$P(w_i) = {V_{tot,m}}^{-1} \bullet \frac{\delta V_i}{\delta w_i} \tag{9}$$

with $V_{tot,m}$ the total mesopore volume, δw_i the i-th pore width increment, $P(w_i)$ the mesopore probability distribution (probability density func-

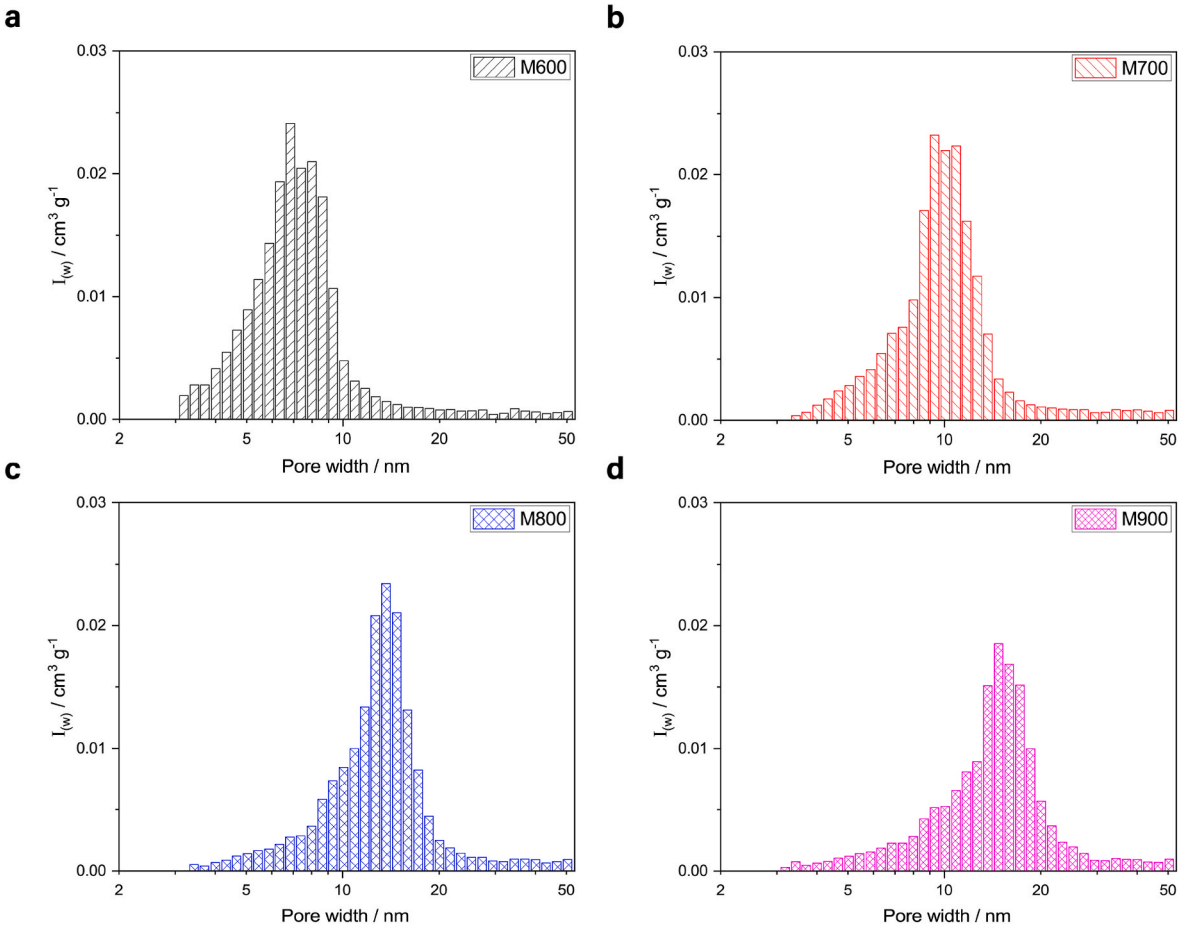

Fig. 7. Mesopore size distributions of the LBM samples, computed by Eq. (7): (a) M600; (b) M700; (c) M800, and (d) M900.

tion), and δV_i as used previously.

The mesopore probability distribution of the samples is reported in Fig. 9. The shift in the distribution peaks at different calcination temperatures can be used to form a hypothesis that, similar to the phase quantification in X-ray powder diffraction, convolution-based profile fitting can be utilized to analyze the homogeneity of the samples. Unlike XRD profiles, there is only one peak in the mesopore probability distributions of the samples. Furthermore, the peaks shorten at higher calcination temperatures and make convolution-based profile fitting less accurate. To overcome this issue, the distributions need to be weighted with a weighting factor. This weighting factor should give higher weights to distributions of higher calcination temperatures. As distribution peaks of the higher calcination temperatures occur at wider pore widths, this study proposes to choose a factor of the pore width ($\ln 10 \bullet w_i$) as the weighting factor.

The weighted mesopore probability distribution is [55]

$$L(w_i) = 2.3\, P(w_i) \bullet w_i \tag{10}$$

or

$$L(w_i) = V_{tot,m}{}^{-1} \bullet \left(2.3\, \frac{\delta V_i}{\delta w_i} \bullet w_i\right) \tag{11}$$

with $L(w_i)$ the weighted mesopore probability distribution, w_i, $P_{(w)}$, $V_{tot,m}$, and δV_i as used previously. Since $2.3 \frac{\delta V_i}{\delta w_i} \bullet w_i$ in Eq. (4.11) is replaceable with $\frac{\delta V_i}{\delta \log(w_i)}$ the proposed equation for weighted mesopore probability distribution, in simplified terms, is

$$L(w_i) = V_{tot,m}{}^{-1} \bullet \frac{\delta V_i}{\delta \log(w_i)} \tag{12}$$

As illustrated by Fig. 10, the weighted mesopore probability distributions' peak heights are almost equal (about 4). This facilitates identifying hidden peaks by deconvolution in inhomogeneous samples. The dashed lines represent the best Lorentz fit to the data. The Lorentz peak function usually is written as

$$y = y_0 + \frac{2A}{\pi} \bullet \frac{W}{\left[4(x - x_c)^2 + W^2\right]} \tag{13}$$

with y_0 the offset from the y-axis, A the area of the function, W the full width at half maximum (FWHM), and x_c the center of the function. All the distributions could be well captured by this function (adjusted R^2 greater than 0.99).

The Lorentz peak functions' parameters, namely center, FWHM, and area, are compared and contrasted in Fig. 11. On the whole, all the parameters increase with the increase in the calcination temperature. For example, the centers of the functions in M600 and M700 are at 7.3 nm and 10.3 nm, respectively, and move to 13.7 nm and 15.4 nm in M800 and M900. The same trend holds true for the area of the functions at different temperatures, as well. Later in this study, the center of these Lorentz fits is used to indicate the calcination temperature of fractions in inhomogeneous samples, and the area of the Lorentz fits is employed to calculate the weight percentages of these fractions.

To verify the methodology, Fig. 12 shows the weighted mesopore probability distribution of the LBM mixtures. The percentage of LBM fractions has been indicated in the mixture designations. For example, M600 (50%)+M900 (50%) is a mixture consisting of 50% M600 and 50% M900. The dashed and dotted lines represent the best Lorentz fits to the data. The properties of each peak are calculated by deconvoluting the distribution by Lorentz peak functions and reiterating peak

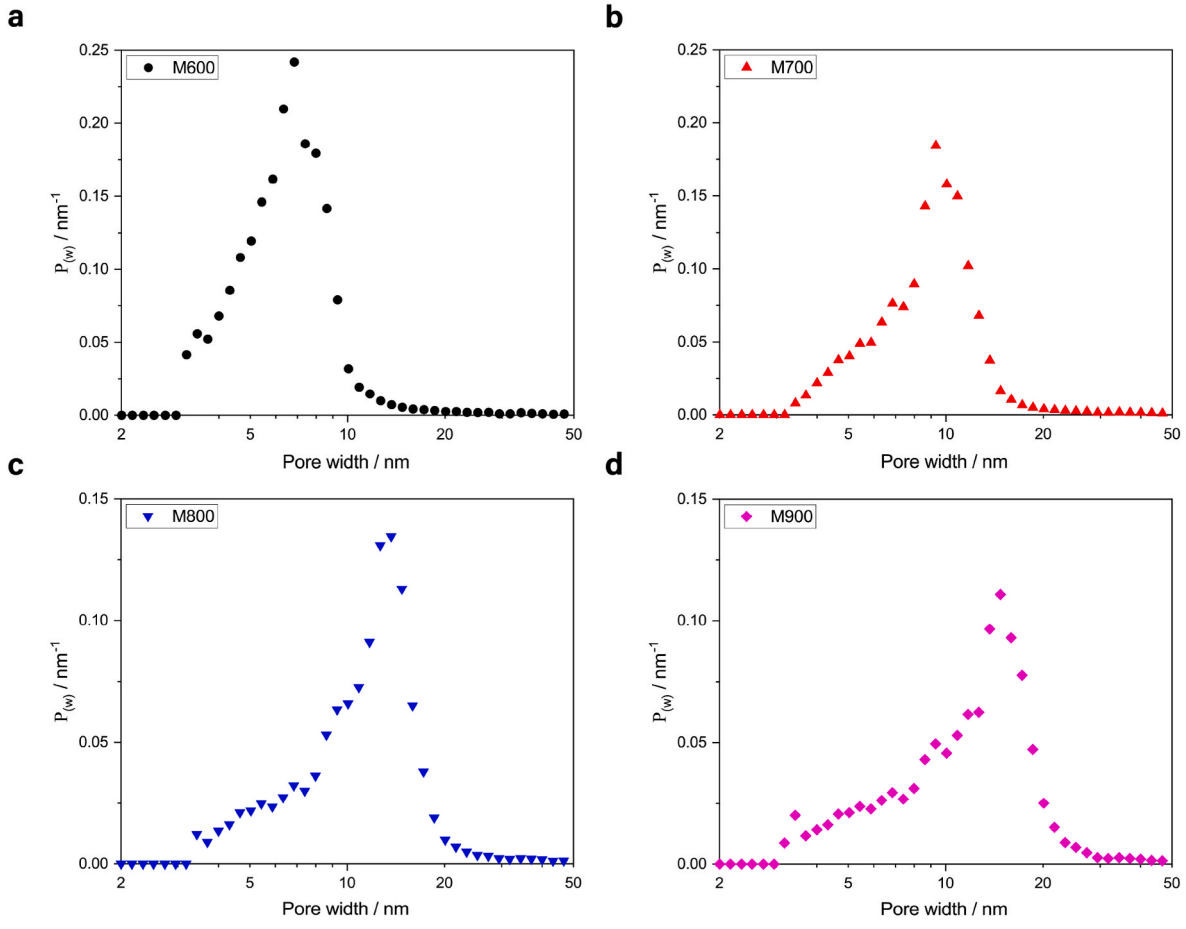

Fig. 9. Mesopore probability distributions of the LBM samples, computed by Eq. (9): (a) M600; (b) M700; (c) M800, and (d) M900.

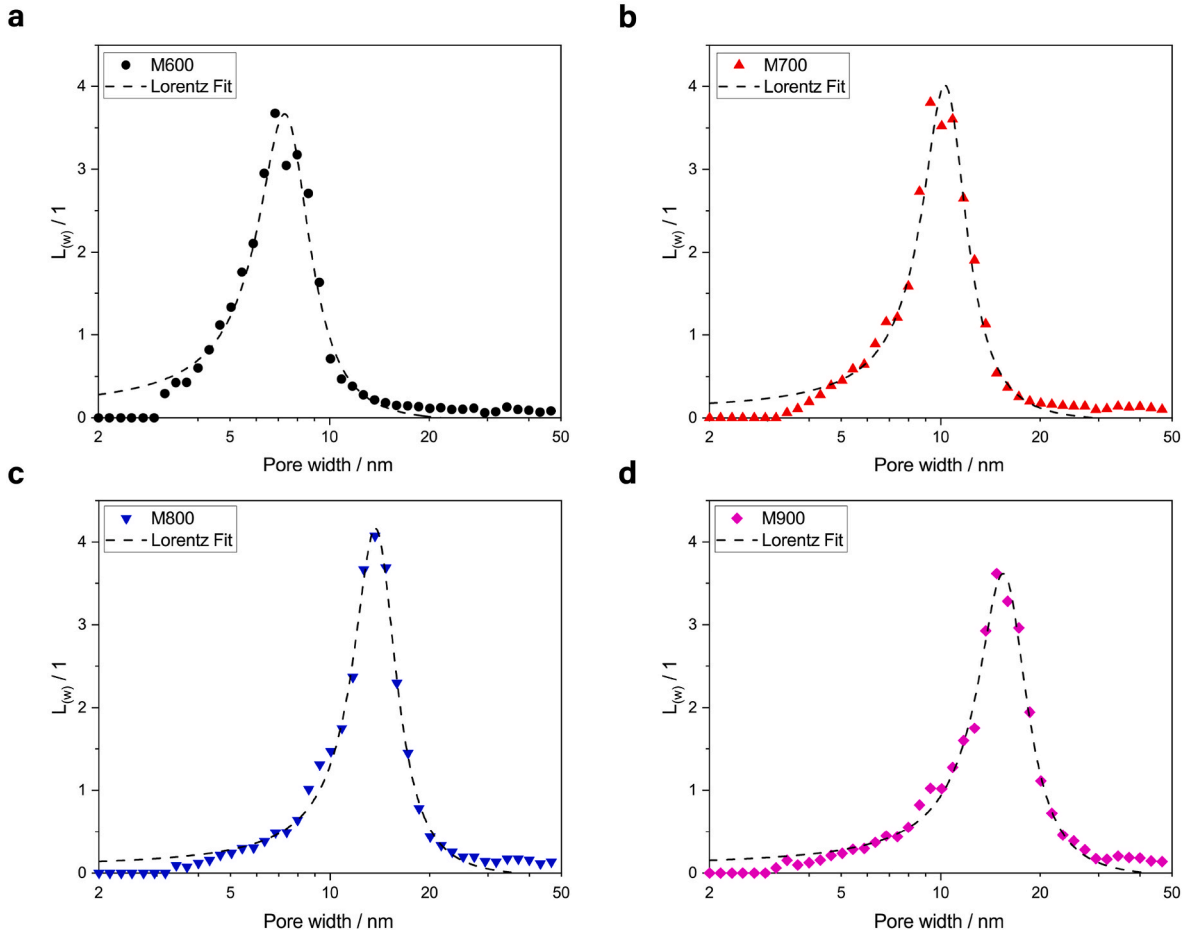

Fig. 10. Weighted mesopore probability distributions of the LBM samples (demonstrated by symbols) and their Lorentz fits (demonstrated by dashed lines), computed by Eq. (12): (a) M600; (b) M700; (c) M800, and (d) M900.

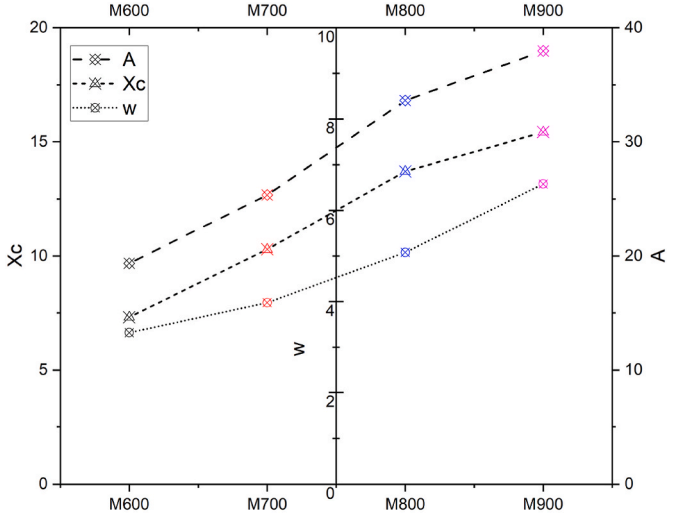

Fig. 11. Parameters of the Lorentz peak functions, taken from Fig. 10. (A: the area of the function, W: the full width at half maximum (FWHM), and Xc: the center of the function).

deconvolution using the Levenberg Marquardt algorithm. All the distributions were well captured by the cumulative fits (adjusted R^2 greater than 0.94).

The centers of the Lorentz fits of Fig. 12 are demonstrated in Fig. 13. The horizontal dashed lines represent the centers of the Lorentz peak functions used for deconvoluting the weighted mesopore probability distributions of unmixed magnesia preparations in Fig. 10. It is evident that the centers of cumulative Lorentz fits are almost identical to those of unmixed LBMs. For example, the centers of the Lorentz fits in both M600 (50%)+M900 (50%) and M600 (80%)+M900 (20%) compare well with the centers of unmixed M600 (7.3 nm) and M900 (15.4 nm). As another example, the centers of the Lorentz fits in both M600 (50%)+M800 (50%) and M600 (80%)+M800 (20%) compare well with the centers of unmixed M600 (7.3 nm) and M800 (13.7 nm), as well. These results provide evidence that deconvoluting the weighted mesopore probability distribution of light-burnt magnesia by Lorentz peak functions is an accelerated method to analyze homogeneity and thermal history.

The percentage of each fraction in LBM mixtures is

$$\text{Fraction i}\,(\%) = \frac{\frac{A^{\,cumulative}_{fraction\ i}}{A^{\,unmixed}_{fraction\ i}}}{\sum_{j=1}^{N} \frac{A^{\,cumulative}_{fraction\ j}}{A^{\,unmixed}_{fraction\ j}}} \tag{14}$$

with $A^{cumulative}_{fraction\ i}$ the area of the i-th Lorentz fit in the cumulative fit (captured from Fig. 12) and $A^{unmixed}_{fraction\ i}$ the area of the i-th Lorentz fit in its unmixed form (captured from Fig. 10).

Table 4 lists the computed percentage of each fraction in LBM mixtures. It is evident that the predicted percentages are in excellent agreement with real values. In addition, these results confirm that the proposed method quantifies the homogeneity of LBM.

LBM mixtures containing M600 and M700 were not studied here since the inhomogeneity caused by a large temperature gap (say M600

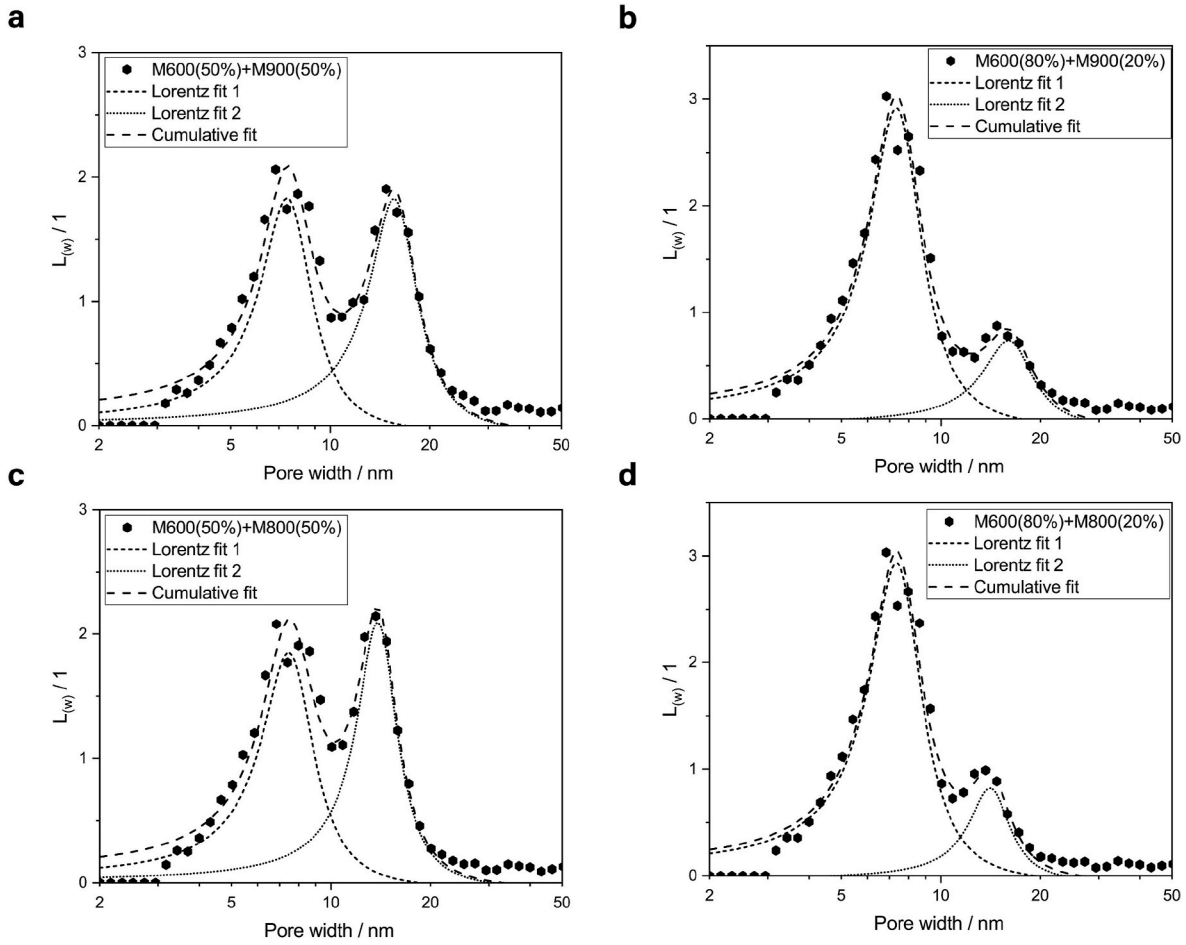

Fig. 12. Weighted mesopore probability distributions of magnesia mixtures and their Lorentz fits: (a) M600 (50%)+M900 (50%); (b) M600 (80%)+M900 (20%); (c) M600 (50%)+M800 (50%), and (d) M600 (80%)+M800 (20%).

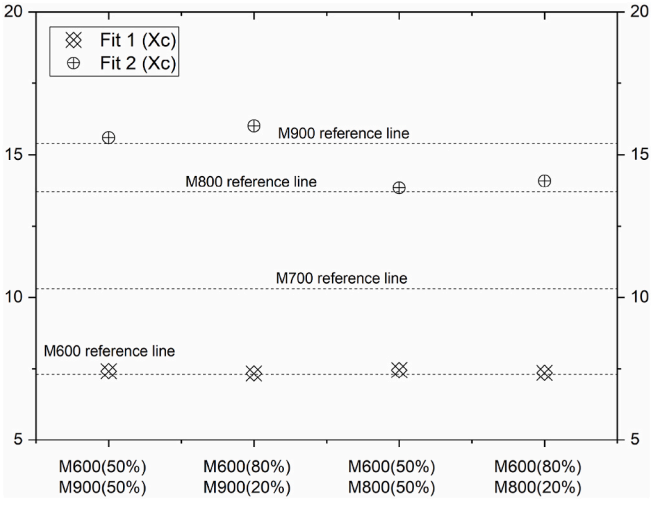

Fig. 13. Center of the Lorentz peak functions used for deconvoluting weighted mesopore probability distributions of magnesia mixtures in Fig. 12. Horizontal dashed lines represent the centers of the Lorentz peak functions used for deconvoluting the weighted mesopore probability distributions of unmixed magnesia preparations in Fig. 10.

and M900 or M600 and M800) is more critical than one caused by a slight temperature gap (say M600 and M700). When the temperature gap is short, the weighted mesopore probability distribution peaks are close. This may not affect the accuracy of the deconvolution method at high inhomogeneity dosages (say 50% M600 plus 50% M700). However, it may reduce its accuracy at low inhomogeneity concentrations (say 80% M600 plus 20% M700).

Table 4
Computed composition of magnesia mixtures versus actual composition.

Mixture	M600 (50%) M900 (50%)	M600 (80%) M900 (20%)	M600 (50%) M800 (50%)	M600 (80%) M800 (20%)
Computed composition (fraction 1)	49.9%	77.5%	51.5%	81.6%
Computed composition (fraction 2)	50.1%	22.5%	48.5%	18.4%

This study indicates the benefits of deconvoluting the weighted mesopore probability distribution by Lorentz peak functions to analyze the homogeneity of light-burnt magnesia. The proposed method is a cost-effective accelerated detection tool for detecting inhomogeneities in light-burnt magnesia. As the pseudomorphous structure of calcined magnesia provides the foundation of this method, the proposed method can be applied to a wide range of pseudomorphous materials to detect inhomogeneities.

However, some limitations are worth noting. This study only analyzed the light-burnt magnesia produced by calcining magnesite. The magnesia produced by calcining other magnesium compounds such as brucite has a different pore structure [41]. Furthermore, the presence of some gases, such as water vapor, may significantly influence the

structure of calcination products [47]. In addition, the presence of impurities in the parent solid may promote sintering [20]. Further research may include the influence of parent solid, impurities in the parent solid, and the calcination atmosphere to provide calibration curves for the method presented here.

4. Conclusions

In this study, a new technique for identifying and quantifying the homogeneity and heat treatment history of light-burnt magnesia (LBM) produced from the calcination of magnesite is reported. The method provides equations (i.e., Eqs. (12) and (14)) for computing the weighted mesopore probability distribution of LBM and analyzing the peaks present in the distribution to examine homogeneity. The properties of each peak are calculated by deconvoluting the distribution by Lorentz peak functions and reiterating peak deconvolution using the Levenberg Marquardt algorithm. Based on the results obtained, the following conclusions can be drawn.

- The proposed method identifies and quantifies the homogeneity and heat treatment history of light-burnt magnesia produced from the calcination of magnesite.
- The method identifies homogeneity by giving the number of fractions from the number of peaks in the weighted mesopore probability distribution. The mixtures containing two LBMs show two peaks in their weighted mesopore probability distributions.
- The method identifies the calcination temperature of each fraction from the center of the Lorentz fit of that fraction in the weighted mesopore probability distribution. The centers of the Lorentz peak functions used for deconvoluting weighted mesopore probability distributions of mixtures containing two LBMs are located very close to the centers of the Lorentz peak functions of their corresponding pure LBMs.
- The method provides the possibility to derive the composition of LBM mixtures using the area of their Lorentz fits in the weighted mesopore probability distribution. The percentage of each fraction in mixtures containing two LBMs are calculated by an equation containing the area of their corresponding Lorentz fits in the mixed and pure LBMs.

Credit author statement

H. Karimi: Conceptualization, Methodology, Investigation, Data curation, Formal analysis, Validation, Visualization, Writing – original draft. H.J.H. Brouwers: Supervision, Funding acquisition, Project administration, Writing – review & editing.

Declaration of competing interest

The authors declare that they have no known competing financial interests or personal relationships that could have appeared to influence the work reported in this paper.

Data availability

Data will be made available on request.

Acknowledgments

This work was supported by the Building Materials sponsor group of Eindhoven University of Technology.

References

[1] M.A. Shand, The Chemistry and Technology of Magnesia, John Wiley & Sons, Inc., Hoboken, NJ, USA, 2006, https://doi.org/10.1002/0471980579.
[2] Future Market Insights, Magnesium Oxide Market. 2021 Analysis and Review: Magnesium Oxide Market by Application – Industrial, Refractories, and Agricultural for 2021-2031, 2021. https://www.futuremarketinsights.com/reports/magnesium-oxide-market.
[3] U.S. Geological Survey, Mineral Commodity Summaries 2021, U.S. Geological Survey, 2021, https://doi.org/10.3133/mcs2021.
[4] M.A.L. Braulio, G.G. Morbioli, L.R.M. Bittencourt, V.C. Pandolfelli, Novel features of nanoscaled particles addition to alumina-magnesia refractory castables, J. Am. Ceram. Soc. 93 (2010) 2606–2610, https://doi.org/10.1111/j.1551-2916.2010.03792.x.
[5] M.A.L. Braulio, V.C. Pandolfelli, Tailoring the microstructure of cement-bonded alumina-magnesia refractory castables, J. Am. Ceram. Soc. 93 (2010) 2981–2985, https://doi.org/10.1111/j.1551-2916.2010.03956.x.
[6] Y. Dai, Y. Li, X. Xu, Q. Zhu, W. Yan, S. Jin, H. Harmuth, Fracture behaviour of magnesia refractory materials in tension with the Brazilian test, J. Eur. Ceram. Soc. 39 (2019) 5433–5441, https://doi.org/10.1016/j.jeurceramsoc.2019.07.026.
[7] Y. Dai, Y. Li, S. Jin, H. Harmuth, Y. Wen, X. Xu, Mechanical and fracture investigation of magnesia refractories with acoustic emission-based method, J. Eur. Ceram. Soc. 40 (2020) 181–191, https://doi.org/10.1016/j.jeurceramsoc.2019.09.010.
[8] E.A. Elkhalifa, H.B. Friedrich, Magnesium oxide as a catalyst for the dehydrogenation of n-octane, Arab. J. Chem. 11 (2018) 1154–1159, https://doi.org/10.1016/j.arabjc.2014.10.002.
[9] E.K. Lee, K.D. Jung, O.S. Joo, Y.G. Shul, Magnesium oxide as an effective catalyst in catalytic wet oxidation of H2S to sulfur, React. Kinet. Catal. Lett. 82 (2004) 241–246, https://doi.org/10.1023/b:reac.0000034833.97966.96.
[10] N. Cooray, Knowledge accumulation and technological advance. The case of synthetic rubber, Res. Pol. 14 (1985) 83–95, https://doi.org/10.1016/0048-7333(85)90016-2.
[11] L. Zhou, S. Zhang, Z. Li, X. Liang, Z. Zhang, R. Liu, J. Yun, Efficient degradation of phenol in aqueous solution by catalytic ozonation over MgO/AC, J. Water Proc. Eng. 36 (2020), 101168, https://doi.org/10.1016/j.jwpe.2020.101168.
[12] X. Yao, N. Jiang, J. Li, N. Lu, K. Shang, Y. Wu, An improved corona discharge ignited by oxide cathodes with high secondary electron emission for toluene degradation, Chem. Eng. J. 362 (2019) 339–348, https://doi.org/10.1016/j.cej.2018.12.151.
[13] H.T.S. Britton, S.J. Gregg, G.W. Winsor, The calcination of dolomite. Part I.—the kinetics of the thermal decomposition of calcite and of magnesite, Trans. Faraday Soc. 48 (1952) 63–69, https://doi.org/10.1039/TF9524800063.
[14] Z.S.H. Abu-Hamatteh, M.A. Alnawafleh, Evaluation of magnesia clinker extracted from dolomite rocks, Miner. Process. Extr. Metall. Rev. 30 (2009) 269–279, https://doi.org/10.1080/08827500802665508.
[15] G. Li, Z. Li, H. Ma, X. Jiang, W. Yao, Preparation of magnesia nanoballs from dolomite, Integrated Ferroelectrics Int. J. 145 (2013) 170–177, https://doi.org/10.1080/10584587.2013.789301.
[16] N.P. Bansal, Sol-gel synthesis of magnesium oxide-silicon dioxide glass compositions, J. Am. Ceram. Soc. 71 (1988) 666–672, https://doi.org/10.1111/j.1151-2916.1988.tb06386.x.
[17] N.P. Bansal, NASA TM-89905 - Sol-Gel Synthesis of MgO-SiO_2 Glass Compositions Having Stable Liquid-Liquid Immiscibility, Pittsburg, Pennsylvania, 1987. https://ntrs.nasa.gov/archive/nasa/casi.ntrs.nasa.gov/19870014317.pdf.
[18] W. Wang, X. Qiao, J. Chen, The role of acetic acid in magnesium oxide preparation via chemical precipitation, J. Am. Ceram. Soc. 91 (2008) 1697–1699, https://doi.org/10.1111/j.1551-2916.2008.02326.x.
[19] J. Adánez, L.F. de Diego, F. García-Labiano, Calcination of calcium acetate and calcium magnesium acetate: effect of the reacting atmosphere, Fuel 78 (1999) 583–592, https://doi.org/10.1016/S0016-2361(98)00186-0.
[20] W.R. Eubank, Calcination studies of magnesium oxides, J. Am. Ceram. Soc. 34 (1951) 225–229, https://doi.org/10.1111/j.1151-2916.1951.tb11644.x.
[21] I.F. Mironyuk, V.M. Gun'ko, M.O. Povazhnyak, V.I. Zarko, V.M. Chelyadin, R. Leboda, J. Skubiszewska-Zięba, W. Janusz, Magnesia formed on calcination of $Mg(OH)_2$ prepared from natural bischofite, Appl. Surf. Sci. 252 (2006) 4071–4082, https://doi.org/10.1016/J.APSUSC.2005.06.020.
[22] V.R. Choudhary, M.Y. Pandit, Surface properties of magnesium oxide obtained from magnesium hydroxide: influence on preparation and calcination conditions of magnesium hydroxide, Appl. Catal. 71 (1991) 265–274, https://doi.org/10.1016/0166-9834(91)85084-9.
[23] F.C. Harper, Effect of calcination temperature on the properties of magnesium oxides for use in magnesium oxychloride cements, J. Appl. Chem. 17 (1967) 5–10, https://doi.org/10.1002/jctb.5010170102.
[24] B. Liu, P.S. Thomas, A.S. Ray, J.P. Guerbois, A TG analysis of the effect of calcination conditions on the properties of reactive magnesia, J. Therm. Anal. Calorim. 88 (2007) 145–149, https://doi.org/10.1007/s10973-006-8106-0.
[25] X. Zhang, Y. Zheng, X. Feng, X. Han, Z. Bai, Z. Zhang, Calcination temperature-dependent surface structure and physicochemical properties of magnesium oxide, RSC Adv. 5 (2015) 86102–86112, https://doi.org/10.1039/C5RA17031A.
[26] F. Demir, B. Dönmez, H. Okur, F. Sevim, Calcination kinetic of magnesite from thermogravimetric data, Chem. Eng. Res. Des. 81 (2003) 618–622, https://doi.org/10.1205/026387603322150462.
[27] A.U. Daniels, R.C. Lowrie, R.L. Gibby, I.B. Cutler, Observations on normal grain growth of magnesia and calcia, J. Am. Ceram. Soc. 45 (1962) 282–285, https://doi.org/10.1111/j.1151-2916.1962.tb11145.x.
[28] C.O. Hulse, S.M. Copley, J.A. Pask, Effect of crystal orientation on plastic deformation of magnesium oxide, J. Am. Ceram. Soc. 46 (1963) 317–323, https://doi.org/10.1111/j.1151-2916.1963.tb11738.x.

[29] A. Cimino, P. Porta, M. Valigi, Dependence of the lattice parameter of magnesium oxide on crystallite size, J. Am. Ceram. Soc. 49 (1966) 152–156, https://doi.org/10.1111/j.1151-2916.1966.tb15394.x.
[30] ACI Committee 212, ACI 212, 3R-16 Report on Chemical Admixtures for Concrete, American Concrete Institute, Farmington Hills, 2016.
[31] S.A. Walling, J.L. Provis, Magnesia-based cements: a journey of 150 Years, and cements for the future? Chem. Rev. 116 (2016) 4170–4204, https://doi.org/10.1021/acs.chemrev.5b00463.
[32] L. Mo, M. Deng, M. Tang, A. Al-Tabbaa, MgO expansive cement and concrete in China: past, present and future, Cement Concr. Res. 57 (2014) 1–12, https://doi.org/10.1016/j.cemconres.2013.12.007.
[33] C. Du, Application of MgO concrete in RCC dams, Concr. Int. 41 (2019) 41–48.
[34] B. Matković, S. Popovic, V. Rogić, T. Žunić, J.F. Young, Reaction products in magnesium oxychloride cement pastes. System MgO-$MgCl_2$-H_2O, J. Am. Ceram. Soc. 60 (1977) 504–507, https://doi.org/10.1111/J.1151-2916.1977.TB14093.X.
[35] F. Cao, M. Miao, P. Yan, Effects of reactivity of MgO expansive agent on its performance in cement-based materials and an improvement of the evaluating method of MEA reactivity, Construct. Build. Mater. 187 (2018) 257–266, https://doi.org/10.1016/J.CONBUILDMAT.2018.07.198.
[36] F. Cao, M. Miao, P. Yan, Hydration characteristics and expansive mechanism of MgO expansive agents, Construct. Build. Mater. 183 (2018) 234–242, https://doi.org/10.1016/J.CONBUILDMAT.2018.06.164.
[37] F. Cao, P. Yan, The influence of the hydration procedure of MgO expansive agent on the expansive behavior of shrinkage-compensating mortar, Construct. Build. Mater. 202 (2019) 162–168, https://doi.org/10.1016/J.CONBUILDMAT.2019.01.016.
[38] L. Mo, M. Deng, M. Tang, Effects of calcination condition on expansion property of MgO-type expansive agent used in cement-based materials, Cement Concr. Res. 40 (2010) 437–446, https://doi.org/10.1016/j.cemconres.2009.09.025.
[39] S. Alegret, M. Blanco, R. Subirats, Potentiometric study of the reactivity of calcined magnesites for use in magnesium oxychloride cements, J. Am. Ceram. Soc. 67 (1984) 579–582, https://doi.org/10.1111/j.1151-2916.1984.tb19597.x.
[40] K. Hirota, N. Okabayashi, K. Toyoda, O. Yamaguchi, Characterization and sintering of reactive MgO, Mater. Res. Bull. 27 (1992) 319–326, https://doi.org/10.1016/0025-5408(92)90061-4.
[41] M.G. Kim, U. Dahmen, A.W. Searcy, Structural transformations in the decomposition of $Mg(OH)_2$ and $MgCO_3$, J. Am. Ceram. Soc. 70 (1987) 146–154, https://doi.org/10.1111/j.1151-2916.1987.tb04949.x.
[42] J. Zhu, N. Ye, J. Liu, J. Yang, Evaluation on hydration reactivity of reactive magnesium oxide prepared by calcining magnesite at lower temperatures, Ind. Eng. Chem. Res. 52 (2013) 6430–6437, https://doi.org/10.1021/ie303361u.
[43] C.K. Chau, Z. Li, Accelerated reactivity assessment of light burnt magnesium oxide, J. Am. Ceram. Soc. 91 (2008) 1640–1645, https://doi.org/10.1111/j.1551-2916.2008.02330.x.
[44] S.J. Gregg, R.K. Packer, The production of active solids by thermal decomposition. Part VI. The calcination of magnesium hydroxide, J. Chem. Soc. (1955) 51–55, https://doi.org/10.1039/jr9550000051.
[45] R.S. Mikhail, S. Nashed, A.M. Khalil, Heats of immersion of pure and doped magnesia in cyclohexane, Effects of micropores, Discuss. Faraday Soc. 52 (1971) 187–195, https://doi.org/10.1039/DF9715200187.
[46] J.P. Coulomb, T.S. Sullivan, O.E. Vilches, Adsorption of Kr, Xe, and Ar on highly uniform MgO smoke, Phys. Rev. B 30 (1984) 4753–4760, https://doi.org/10.1103/PhysRevB.30.4753.
[47] M.R. Carrott, P. Carrott, M.B. De Carvalho, K.S.W. Sing, Ex-hydroxide magnesium oxide as a model adsorbent for investigation of micropore filling mechanisms, J. Chem. Soc. Faraday. Trans. 87 (1991) 185–191, https://doi.org/10.1039/FT9918700185.
[48] J. Rouquerol, F. Rouquerol, P. Llewellyn, G. Maurin, K.S.W. Sing, Adsorption by Powders and Porous Solids: Principles, Methodology and Applications, second ed., second ed., Academic Press, 2013 https://doi.org/10.1016/C2010-0-66232-8.
[49] J. Landers, G.Y. Gor, A.V. Neimark, Density functional theory methods for characterization of porous materials, Colloids Surfaces A Physicochem. Eng. Asp. 437 (2013) 3–32, https://doi.org/10.1016/j.colsurfa.2013.01.007.
[50] E.A. Payzant, Other topics, in: Princ. Appl. Powder Diffr., John Wiley & Sons, Ltd, Chichester, UK, 2009, pp. 365–380, https://doi.org/10.1002/9781444305487.ch9.
[51] P. Webb, C. Orr, Analytical Methods in Fine Particle Technology, 1997. Norcross, GA.
[52] S.J. Gregg, K.S.W. Sing, Adsorption, Surface Area and Porosity, 2 ed., Academic Press, London, 1982.
[53] M.R. Bhambhani, P.A. Cutting, K.S.W. Sing, D.H. Turk, Analysis of nitrogen adsorption isotherms on porous and nonporous silicas by the BET and α_s methods, J. Colloid Interface Sci. 38 (1972) 109–117, https://doi.org/10.1016/0021-9797(72)90226-3.
[54] M. Thommes, K. Kaneko, A. V Neimark, J.P. Olivier, F. Rodriguez-Reinoso, J. Rouquerol, K.S.W. Sing, Physisorption of gases, with special reference to the evaluation of surface area and pore size distribution (IUPAC Technical Report), Pure Appl. Chem. 87 (2015) 1051–1069, https://doi.org/10.1515/pac-2014-1117.
[55] K. Meyer, P. Klobes, Comparison between different presentations of pore size distribution in porous materials, Fresenius' J. Anal. Chem. 363 (1999) 174–178, https://doi.org/10.1007/s002160051166.
[56] J.H. de Boer, B.G. Linsen, Physical and chemical aspects of adsorbents and catalysts, Z. Phys. Chem. 80 (1972), https://doi.org/10.1524/zpch.1972.80.1_2.107, 107–107.
[57] D. Nicholson, Variation of surface area during the thermal decomposition of solids, Trans. Faraday Soc. 61 (1965) 990–998, https://doi.org/10.1039/tf9656100990.